Materials Today Energy 41 (2024) 101525

Contents lists available at ScienceDirect

Materials Today Energy

journal homepage: www.journals.elsevier.com/materials-today-energy/

Electrochemical reduction of NO_3^- to NH_3 using defect-rich TiO_2 support loaded with CuNi catalysts: differential electrochemical mass spectrometry insights

Eleazar Castañeda-Morales [a], José Oziel Peralta-Cruz [b], Francisco Ruiz-Zepeda [c, d], Arturo Susarrey-Arce [e, ***], Martha Leticia Hernández-Pichardo [b, **], Arturo Manzo-Robledo [a, *]

[a] Instituto Politécnico Nacional, Laboratorio de Electroquímica y Corrosión. Escuela Superior de Ingeniería Química e Industrias Extractivas, Av. Instituto Politécnico Nacional S/N, Unidad Profesional Adolfo López Mateos, CP 07708 CDMX, Mexico
[b] Instituto Politécnico Nacional, Laboratorio de Nanomateriales Sustentables, Escuela Superior de Ingeniería Química e Industrias Extractivas, Av. Instituto Politécnico Nacional S/N, Unidad Profesional Adolfo López Mateos, CP 07708 CDMX, Mexico
[c] Department of Materials Chemistry, National Institute of Chemistry, Hajdrihova 19, Ljubljana 1000, Slovenia
[d] Department of Physics and Chemistry of Materials, Institute of Metals and Technology, Lepi Pot 11, Ljubljana, Slovenia
[e] Mesoscale Chemical Systems, MESA+ Institute, University of Twente, PO Box 217, Enschede 7500 AE, the Netherlands

ARTICLE INFO

Article history:
Received 6 October 2023
Received in revised form
9 January 2024
Accepted 8 February 2024
Available online 13 February 2024

Keywords:
NO_3^- electroreduction reaction
Defect-rich titanium dioxide
Ammonia
DEMS
CuNi

ABSTRACT

A promising approach for reducing nitrate (NO_3^-) in water waste is NO_3^- reutilization to ammonia (NH_3). This work investigates the synergistic effect of $Cu_{40}Ni_{60}$ catalyst on a defect-rich TiO_2 (TNSD) carbon vulcan composite (C-TNSD). The study starts with CuNi metallic content pre-screened over carbon vulcan (C) to identify the most promising CuNi ratios for nitrate reduction reaction (NO_3-RR) to NH_3. This is the case of Cu 20 wt% and Ni 80 wt% ($Cu_{20}Ni_{80}$), Cu 40 wt% and Ni 60 wt% ($Cu_{40}Ni_{60}$), Cu 60 wt% and Ni 40 wt % ($Cu_{60}Ni_{40}$), and Cu 80 wt%, Ni 20 wt% ($Cu_{80}Ni_{20}$) and Cu/Ni monometallic catalysts. Among these ratios, $Cu_{40}Ni_{60}$ resulted in the most promising electrocatalyst when loaded over C-TNSD, whose functionality has been assessed using *in situ* differential electrochemical mass spectrometry (DEMS). The results indicate that $Cu_{40}Ni_{60}$/C-TNSD attains a similar NH_3 selectivity to $Cu_{40}Ni_{60}$ supported on TiO_2-carbon vulcan composites. However, $Cu_{40}Ni_{60}$/C-TNSD does not hinder charge transport, making it the most suitable electrocatalyst for NH_3 production. A synergistic interaction between $Cu_{40}Ni_{60}$ and C-TNSD is proposed. The results are supported by structural, (electro)chemical, and morphological characterization. From a broader perspective, defective-rich catalysts can be developed to control the electrochemical reaction sequence during NO_3-RR.

1. Introduction

Nitrate is one of the most common pollutants in water sources, and its high levels can cause eutrophication, harmful effects on aquatic life, and health problems for humans [1]. A promising approach for reducing nitrate (NO_3^-) content in water is NO_3^- reutilization to higher-value products like NH_3. For NH_3, ambitious objectives have been established to reduce the still-high H_2 demand from fossil sources by integrating H_2 into the NH_3 process using environmentally friendly alternatives, such as green hydrogen from alkali electrolysis [2]. Another alternative for NH_3 production is the electrochemical reduction of NO_3^-. The approach is a sustainable and environmentally friendly scheme where electricity is used to reduce NO_3^- from water waste to NH_3, a crucial chemical unit for fertilizers [3].

Recycling NO_3^- from waste to NH_3 can further help reduce fertilizer dependency on the energy-intensive and environmentally harmful Haber–Bosch (HB)-NH_3 process and potentially close the loop in the nitrogen cycle [4,5]. Hence, we expect that NH_3-based fertilizers produced during the electrochemical reduction of NO_3^-

* Corresponding author.
** Corresponding author.
*** Corresponding author.
E-mail addresses: a.susarreyarce@utwente.nl (A. Susarrey-Arce), mhernandezp@ipn.mx (M.L. Hernández-Pichardo), amanzor@ipn.mx (A. Manzo-Robledo).

https://doi.org/10.1016/j.mtener.2024.101525

will be applied to agricultural soils, supplying plants with essential nutrients. Fertilizers will break down into oxidized nitrogenated molecules, releasing NO_3^- which can then be captured for NH_3 electrosynthesis. Ideally, this will create a sustainable nitrogen cycle where NO_3^- can be converted to NH_3, used in fertilizers, and returned as NO_3^-. Other oxidized nitrogenated species might be produced during NO_3^- reaction (e.g., NO_2^-) which needs to be considered [6–8].

The proposed electrochemical approach offers the opportunity to mitigate the negative environmental impacts of conventional fertilizer products. Several steps might be required to fulfill this purpose, but if achieved, NO_3^--recycling can further benefit the NH_3 dependency of the fertilizer industry. A decrease in HB-NH_3 has further benefits. NO_3^- conversion to NH_3 can reduce the HB energy penalty, which uses around 2% of the world's energy annually [5]. At the molecular level, the energy penalty of the HB is ascribed to the high dissociation energy of the triple nitrogen bond (N ^ N), close to 941 kJ/mol [9]. NO_3^- is an exciting nitrogen source because N]O has a relatively lower dissociation energy (204 kJ/mol) than NH_3. Furthermore, less HB-NH_3 dependency will subsequently reduce the CO_2 footprint. Without a change in the current NH_3 manufacturing process, emissions of ~450 million metric tons of CO_2 per year are expected by 2050—a critical scenario for the transforming chemical industry [5].

Materials for the transforming chemical industry should also be adapted to accomplish the energy transition goal. This is the case of electrocatalysts, which should preferably be earth-abundant, as in the case of nickel (Ni) and copper (Cu). Cu [10–12], and Ni [13] have been investigated for the electrochemical reduction of NO_3^- to NH_3. Cu catalysts have a strong adsorption affinity for NO_3^-. To achieve high faradaic efficiency for NH_3 (FE_{NH3}) exceeding 90% during NO_3^- reduction reaction (NO_3-RR) in alkaline conditions, the Cu catalysts must operate at cathodic potentials near (or largely negative than) −0.27 V vs. reversible hydrogen electrode (RHE). However, this cathodic potential requirement could result in a significant overpotential of over 1 V, leading to parasitic reaction competition (e.g., hydrogen evolution reaction, HER).

Higher activity at relatively lower cathodic potentials can be achieved with Cu by changing the adsorption characteristics of the metal and, thus, intermediates by weakening NO_3^--adsorbed species binding energies. One strategy is combining Cu with other metals. For example, CuNi alloys and other co-catalyst mixtures can positively shift the NO_3^- reduction at lower overpotentials. In this case, Cu allows NO_3^--adsorption, while Ni is the binding site for hydrogenation, which in some cases has been suggested to form a hydride intermediate at cathodic potentials [14]. A synergistic effect between Cu and Ni can lead to NO_3^--hydrogenation, increasing the selectivity of NO_3^- to NH_3 [15–17].

The mechanism responsible for NO_3^- reduction has been elucidated for CuNi, whose electronic structure varies depending on the metal ratios [9,17]. For multimetallic compositions, not necessarily alloys, NO_3^- selectivity toward NH_3 has been attributed to a synergistic effect between two metals [18]. In the case of CuNi and defect-rich metal oxide supports, synergy can be expected as combined form can increase electron transfer by applying a cathodic potential, providing enough active sites for NO_3-RR [6–8,19]. Recently, it has been demonstrated electrochemically that defects, e.g., oxygen vacancies (OVs), can promote the formation of active sites to facilitate NO_3-RR [19–22]. This has been the case with TiO_2 support used to host single elemental compositions, like Cu on TiO_2 [11]. However, the synergy between CuNi and defect-rich engineered supports remains unexplored, particularly during the sequential evaluation of chemical products using DEMS.

This work investigates the synergistic effect of CuNi supported on defect-rich TiO_2 nanosheet composites. CuNi metallic contents have been pre-screened over C to identify the most promising CuNi compositions for NO_3-RR to NH_3. In total, four metal combinations containing different wt.% ratios have been used. This is the case of $Cu_{20}Ni_{80}$, $Cu_{40}Ni_{60}$, $Cu_{60}Ni_{40}$, $Cu_{80}Ni_{20}$, and Cu and Ni as controls. $Cu_{40}Ni_{60}$ resulted in the most promising electrocatalyst and thus further studied over TiO_2. Hence, $Cu_{40}Ni_{60}$ supported on C-TNSD is synthesized ($Cu_{40}Ni_{60}$/C-TNSD). The $Cu_{40}Ni_{60}$/C-TNSD DEMS results are contrasted with commercial TiO_2 (T0) and TiO_2 nanosheets (TNS). DEMS reveals that nitrogen species, such as NO and N_2O, can be generated over multiple supports, i.e., carbon vulcan (C), C-T0, C-TNS, and C-TNSD. $Cu_{40}Ni_{60}$, loaded over the latest supports, modifies the NO_3-RR reaction pathway, forming NO, N_2O, and NH_3. Among the electrocatalysts, we identified that $Cu_{40}Ni_{60}$ over C-TNS and $Cu_{40}Ni_{60}$/C-TNSD attained a similar activity toward NH_3. Nevertheless, the $Cu_{40}Ni_{60}$ over C-TNS shows a plateau that hinders charge transport, making $Cu_{40}Ni_{60}$/C-TNSD the most suitable electrocatalyst for NH_3. Impedance measurements demonstrate that charge transfer issues are mitigated with C-TNSD. Our results are supported by structural, (electro)chemical, and morphological characterization of the multiple supports loaded with $Cu_{40}Ni_{60}$, which reveal a synergistic effect between $Cu_{40}Ni_{60}$ and the defective-rich TiO_2. From a broader perspective, defective-rich catalysts can be developed to control the electrochemical reaction sequence during NO_3-RR.

2. Experimental section

2.1. Synthesis of TiO_2 nanosheets

TiO_2 nanosheets were synthesized by the hydrothermal method using titanium butoxide (TiBu) at 97% purity in 70 wt% HF. The volume ratio between TiBu and hydrofluoric acid (HF) was maintained at 3:25, and this solution was stirred for 2 h. The obtained mixture was transferred to a 100 mL Teflon-lined stainless-steel autoclave and placed in an oven at 180 °C for 36 h. After hydrothermal treatment, the reaction system was cooled down to room temperature. The resulting mixture was a beige-colored mixture, which was washed and filtered. The impurities were removed using a solution prepared with ethanol and distilled water. The filtrate was then dispersed in a 0.01 M NaOH solution and stirred for 8 h at atmospheric conditions. A second washing process, followed by filtration, was carried out. Finally, TNS were dried in an oven at 80 °C for 6 h. TNSD was obtained by treating the TNS thermally in a reduced atmosphere for 2 h at 200 °C in 4% H_2 diluted in Ar.

2.2. Synthesis of supported CuNi on carbon-TiO_2

The synthesis of Cu, Ni, and CuNi supported on C–TiO_2 composites started by preparing a suspension using $NiCl_2$ and $CuCl_2$ as metallic precursors in 100 ml of CH_3OH. The suspension was stirred at 65 °C for 1 h in an Ar atmosphere. After that, 50 ml of $NaBH_4$ was added to the suspension. Cu, Ni, and CuNi wt.% combinations (i.e., $Cu_{20}Ni_{80}$, $Cu_{40}Ni_{60}$, $Cu_{60}Ni_{40}$, $Cu_{80}Ni_{20}$) were supported on the electrocatalyst, i.e., C, C-TNS, C-TNSD, or C-T0 carefully maintaining a metal:support ratio at 1:9. It should be noted that the C and TiO_2 composite ratio was maintained at 7:3.

2.3. Structural and morphological characterization

The catalysts were characterized with (i) X-ray diffraction (XRD), (ii) X-ray photoelectron spectroscopy (XPS), and (iii) scanning/transmission electron microscopy (S/TEM). (i) XRD from PANalytical model X Pert PRO fitted with a PiXcel detector was used to analyze the crystallographic phase of all samples. (ii) XPS was used to investigate the chemical surface environment of the

electrocatalyst and was done with a K-alpha Thermo Fischer Scientific spectrometer with a monochromatic Al Kα source (1486.6 eV). Samples remained under vacuum for more than 10 h in a pre-chamber directly connected to the equipment and then transferred to the analysis chamber zone with a base pressure of 1×10^{-9} Torr that remained constant throughout the experiment. (iii) Scanning transmission electron microscopy (STEM) and energy-dispersive X-ray spectrometry (EDXS) observations were done in a Cs-corrected microscope JEOL ARM 200CF equipped with a JEOL SSD EDX spectrometer and a Gatan Dual EELS Quantum spectrum imaging filter. The operational voltage was set to 80 kV. The catalyst powders were dispersed in ethanol and deposited over a holey carbon-coated Au grid.

2.4. Electrochemical characterization

Electrochemical measurements were performed using a potentiostat–galvanostat (Autolab PSGSTAT-302) in a three-electrode cell setup. The electrodes used were a platinum wire as a counter electrode (CE), a standard hydrogen electrode (SHE, prepared with H_2SO_4 0.5 M) as reference electrode (RE), and glassy carbon (GC, 3 mm in diameter) as the working electrode (WE). The GC electrode was polished with a 0.05 μm Al_2O_3 powder to a mirror-finished surface. A homogeneous ink was prepared by a mixture of 5 mg of electrocatalyst in 1 ml of solution (75:25 water: isopropanol) and 70 μl of 5% wt Nafion in an ultrasonic bath for 30 min. The glassy carbon electrode was coated with 5 μl of the suspension and dried at room temperature. The total electrocatalyst mass load for all experiments was 0.33 $mg_{catalyst}/cm^2$. All measurements were carried out with a standard hydrogen electrode (SHE). The recorded values were then converted to the reversible hydrogen electrode according to $E_{RHE} = E^{\circ}_{SHE} + E_{SHE} + 0.059\ pH$. For the SHE electrode, $E^{\circ}_{SHE} = 0$ V, the pH solution was determined by the pH-meter Orion 420A+. The electrochemical technique employed to evaluate the electrocatalytic activity was cyclic voltammetry carried out in the potential window from 0.4 −1.4 V vs. SHE with a scan rate of 20 mV/s. An aqueous 1 M NaOH solution saturated with Ar was used as a supporting electrolyte. Cyclic voltammetry was employed to determine the electrochemically active surface area (ECSA) and capacitance values. ECSA measurements were carried out in the presence of 1 M *KCl* solution with 10 mM $K_3Fe(CN)_6$ in scan rates between 25 and 150 mV/s. Capacitance values were determined at 1 M NaOH solution in the potential window from 0.3 to 0.4 V vs. SHE in scan rates between 75 and 500 mV/s. Charge transport processes in steady state technique were studied using electrochemical impedance spectroscopy (EIS) measurements. This analysis was carried out for each supporting electrolyte, applying a sinusoidal signal of 10 mV of amplitude in the frequency range from 10^5 to 0.1 Hz at an applied potential of −1.1 V vs. SHE for $Cu_{40}Ni_{60}$ loaded over the multiple C–TiO_2 supports in NaOH 1 M solution without and with 0.1 M $NaNO_3$. All experiments were performed at room temperature, and the solutions were saturated with Ar for 15 min before polarization.

2.5. In situ DEMS

An electrochemical reactor for a three-electrode setup was used to record the ionic and faradaic currents as a function of electrode potential (and time). The electrochemical measurements were performed using a potentiostat–galvanostat (μAutolab III). The cell components (WE, CE, RE, and electrolyte) employed for DEMS analysis were as described for electrochemical characterization in Section 2.4. The ionic current (mass signal) for selected mass-to-charge ratios (m/z) and the current–potential profiles were recorded simultaneously at a scan rate of 1 mV/s. The experiments were carried out in a potential window from 0 to −1.2 V vs. SHE for $Cu_{40}Ni_{60}$/C-T0, $Cu_{40}Ni_{60}$/C-TNS, and $Cu_{40}Ni_{60}$/C-TNSD from 0 to −1.5 V vs. SHE in NaOH 1 M in the presence of $NaNO_3$ (0.1 M). In all cases, the total electrocatalyst mass load for all experiments was 0.33 $mg_{catalyst}/cm^2$. The electrochemical cell was connected to the quadrupole mass spectrometer (Prisma QMG220) at a working pressure of ca. 2.7×10^{-5} mbar. All solutions were purged with Ar prior to the DEMS analysis.

3. Results and discussion

3.1. $Cu_{40}Ni_{60}$ electrocatalyst optimization

This study starts with the synthesis of CuNi supported on carbon vulcan (CuNi/C) using various CuNi wt.% ratios: $Cu_{20}Ni_{80}$, $Cu_{40}Ni_{60}$, $Cu_{60}Ni_{40}$, $Cu_{80}Ni_{20}$, and monometallic Cu and Ni. The catalyst is electrochemically evaluated in alkaline conditions in the presence and absence of $NaNO_3$, as shown in Fig. S1. The results in Fig. S1 demonstrate that the $Cu_{40}Ni_{60}$/C electrocatalyst has the highest faradaic current in the redox peak associated with NO_3-RR. Therefore, the $Cu_{60}Ni_{40}$ ratio has been used to prepare a $Cu_{40}Ni_{60}$ supported on C–TiO_2 composites to investigate the synergy between $Cu_{40}Ni_{60}$ and TiO_2. Thus, the metallic ratio ($Cu_{40}Ni_{60}$) has been used to prepare electrocatalysts loaded over C-T0, C-TNS, and C-TNSD composites. The electrocatalysts are labeled as $Cu_{40}Ni_{60}$/C-T0, $Cu_{40}Ni_{60}$/C-TNS, and $Cu_{40}Ni_{60}$/C-TNSD.

3.2. Morphological and structural characterization

The XRD patterns of the $Cu_{40}Ni_{60}$ prepared with different supports are shown in Fig. 1 (a-b). Fig. 1 reveals that the XRD patterns present several diffraction peaks corresponding to the different metals and oxides of Cu and Ni, along with the diffraction signals of carbon vulcan (C) and TiO_2 supports. All the electrocatalysts loaded over C presented two broad signals at $2\theta \approx 24.8$ and 43.4, corresponding to C (002) and C (100), with a graphite-like structure (JCPDS 41–1487) (Fig. S2). As for the C–TiO_2 supports, the C-TNSD, C-TNS, and C-T0 electrocatalyst shows the characteristic TiO_2 diffraction peaks at $2\theta \approx 25.4$, 37.7, 48.1, 54.0, 55.1, 62.7, 68.7, 70.4, and 75.3 attributed to the (101), (004), (200), (105), (211), (204), (116), (220), and (215), planes of the anatase phase (JCPDS 21–1272) [23]. Contrary to the synthesized C-TNSD and C-TNS, C-T0 shows intense sharp peaks, indicating that TiO_2 is highly crystalline. The composites prepared with C-TNSD and C-TNS display line broadening of the peaks due to the polymorphic structure of the nanosheets, which suggests the presence of small particle sizes. A close look at the diffraction peaks in Fig. 1(b) shows species $Cu_{40}Ni_{60}$ present over the various C-TNSD, C-TNS, and C-T0 supports. The monometallic copper displayed three XRD peaks at $2\theta = 43.4$ and 50.5, characteristic of the face-centered-cubic (fcc) for the planes (111) and (200) (JCPDS 04–0836) [23]. A detailed analysis for C reveals a slight decrease in Cu lattice spacings when Ni is present (Fig. S2), suggesting that our Cu and Ni co-catalysts could be partially alloyed [24]. On the other hand, $Cu_{40}Ni_{60}$/C and $Cu_{40}Ni_{60}$/C-T0 exhibited two peaks appeared at $2\theta = 44.4$ and 51.7, which corresponds to the (111) and (200) planes (JCPDS 04–0850) for Ni (fcc) [25]. The results indicate that CuNi species on TNSD and TNS resemble the CuNi species over C (Fig. S2). CuNi species are identified as a combination of metal and metal oxides in Fig. 1(b).

$Cu_{40}Ni_{60}$ electrocatalyst structural, morphological, and chemical characteristics are studied with STEM and STEM-EDX (Fig. 2). In Fig. 2(a) and **(2a′)**, oxidized Ni (denoted in bright color and highlighted with yellow arrows) has been found with a nanoweb-like shape over the C support. Ni species can be in the form of oxide or hydroxide (Fig. 2(a)), as will be discussed below (see XPS

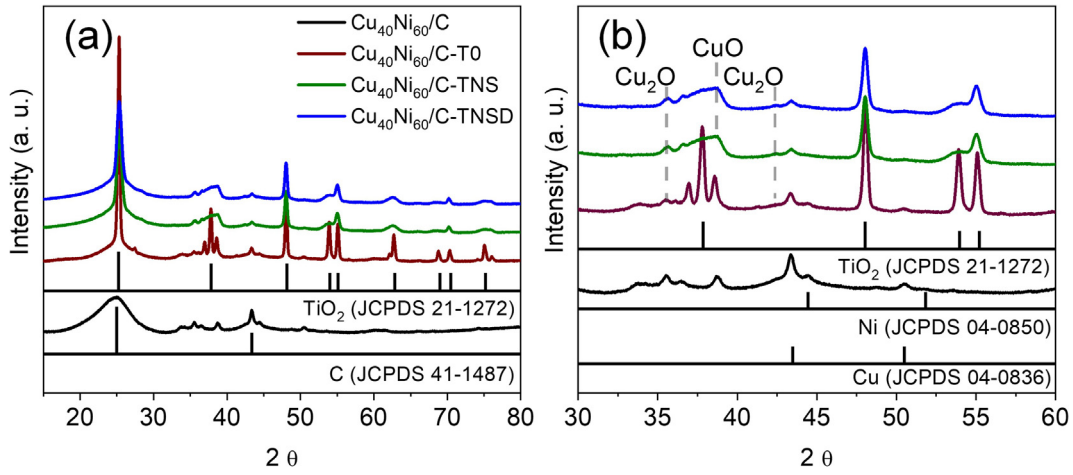

Fig. 1. (a) XRD patterns of $Cu_{40}Ni_{60}$/C and $Cu_{40}Ni_{60}$/C—TiO_2 electrocatalysts (C, C-T0, C-TNS, and C-TNSD). C and A-labels refer to carbon vulcan and TiO_2 anatase. (b) Enlarged view of the main Ni and Cu species peaks region.

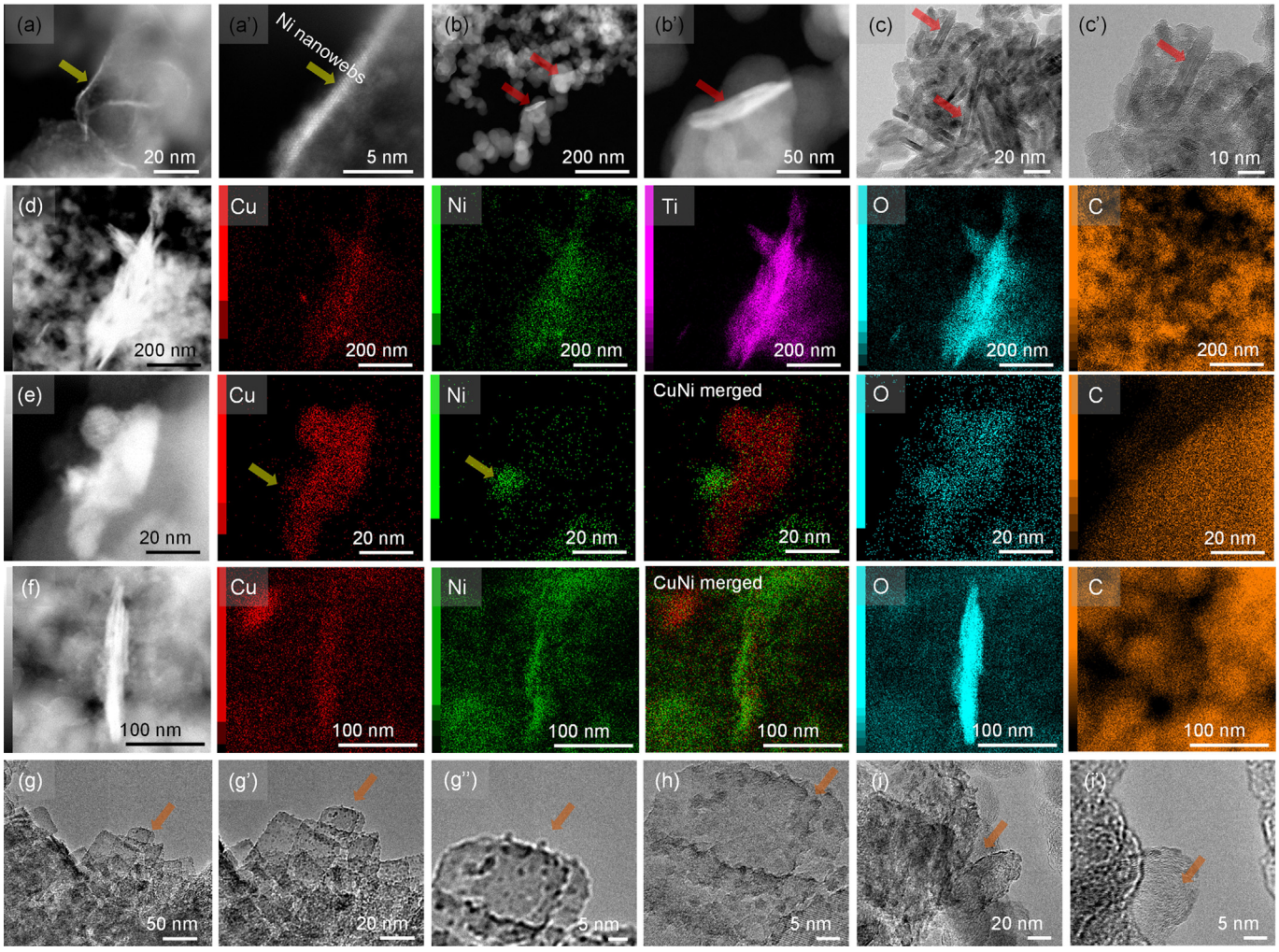

Fig. 2. STEM-ADF imaging of (a, a') $Cu_{40}Ni_{60}$/C, (b, b') $Cu_{40}Ni_{60}$/C-TNS. TEM imaging of (c, c') $Cu_{40}Ni_{60}$/C-TNSD. STEM-ADF and EDXS maps of (d, e) $Cu_{40}Ni_{60}$/C-TNS and (f) $Cu_{40}Ni_{60}$/C-TNSD after the NO3-RR. TEM imaging of (g, g', g'') $Cu_{40}Ni_{60}$/C-TNSD, (h) $Cu_{40}Ni_{60}$/C-TNSD, (i, i') $Cu_{40}Ni_{60}$/C-TNSD.

analysis). On the other hand, Cu has been found dispersed over the support, forming aggregates. Over the C-TNS, Ni-like nanowebs are observed in Fig. 2(a'). As for TiO_2, C-TNS have TiO_2 nanosheet morphology, as shown in Fig. 2(b) and **(b')**. The results for TiO_2 nanosheet-like morphology also agree for C-TNSD (Fig. 2(c) and **(c')**), where the tiny crystals have been observed.

For $Cu_{40}Ni_{60}$/C-TNS electrocatalyst, Cu (red), Ni (green), Ti (purple), O (blue), and C (carbon), STEM-EDX elemental maps are

shown in Fig. 2(d) and **(e)**. In this case, Cu is observed as aggregates over the C-TNS, which is also the case for Ni. Although STEM-EDX reveals the presence of aggregates, CuNi EDX signals also overlap, as found in Fig. 2(e) (yellow arrows). After the NO_3-RR, we analyze $Cu_{40}Ni_{60}$/C-TNSD. Similar results to Fig. 2(d and e) are observed in Fig. 2(f), where Cu and Ni are distributed across the electrocatalyst. CuNi segregation can be attributed to the oxidized Cu and Ni. In the same figure, Ni nanowebs can be assessed by looking at the merged NiCu image, where a slightly more significant EDX-Ni signal has been observed. O and C have also been included to demonstrate the presence of oxidized Cu and Ni and the existence of carbon. Detailed TEM analysis of the $Cu_{40}Ni_{60}$/C-TNSD after NO_3-RR is also shown in Fig. 2(g), **(g')**, **(g")**, and **(h)**. Particle-like shapes are found distributed over C-TNSD. The presence of graphitic carbon in Fig. 1 is confirmed in Fig. 2(i) and **(i')**.

The chemical environment of (a) Cu, (b) Ni, (c) Ti, and (d) O in $Cu_{40}Ni_{60}$/C-TNSD, $Cu_{40}Ni_{60}$/C-TNS, $Cu_{40}Ni_{60}$/C-T0, and $Cu_{40}Ni_{60}$/C are evaluated to provide insights on the nature of the chemical species present at the electrocatalyst surface (Fig. 3). Fig. 3(a) shows the peak fitting for the Cu $2p_{3/2}$ core level. The Cu $2p_{3/2}$ spectrum has been deconvoluted into three peaks at about 932.5 eV, 933.8 eV, and 935.2 eV assigned to the formation of Cu_2O, CuO, and $Cu(OH)_2$, along with two satellites at about 941.2 eV and 943.7 eV [26]. The effect of the chemical environment from the TiO_2 is observed when compared with C support. Cu-supported over C−TiO_2 reveals an energy shift of +1 eV. Fig. 3(b) shows the peak fit for the Ni $2p_{3/2}$ core level. The spectrum is deconvoluted into two peaks at about 855.7 eV and 857.3 eV along with the satellite which can be attributed to the chemical states of nickel, such as Ni, Ni^{2+} in the form of NiO, and Ni^{2+} in the form of $Ni(OH)_2$ [27]. Overall, the results indicate the existence of oxidized Ni and Cu species over the various supports.

Fig. 3(c) displays the Ti 2p spectra for the $Cu_{40}Ni_{60}$/C-TNSD, $Cu_{40}Ni_{60}$/C-TNS, $Cu_{40}Ni_{60}$/C-T0, and $Cu_{40}Ni_{60}$/C electrocatalysts. The electrocatalysts revealed XPS peaks at about 464.5−464.9 eV and 458.6−459.1 eV, corresponding to the Ti^{4+} oxidation state. Other Ti 2p peaks are located at about 458.1−463.7 eV and correspond to the Ti^{3+} species [28]. It should be noted that the peak-splitting for the Ti $2p_{1/2}$ and Ti $2p_{3/2}$ signals is $\Delta = 5.7$ eV, in agreement with metal oxide electrocatalysts. Furthermore, the corresponding areas for the different Ti species showed that the Ti^{3+} is around 50.3, 37.7, and 19.7% for $Cu_{40}Ni_{60}$/C-TNSD, $Cu_{40}Ni_{60}$/C-TNS, and $Cu_{40}Ni_{60}$/C-T0, suggesting the presence of uncoordinated Ti species. Table 1 shows the relative contents of Ti^{3+} and the peak area ratio of Ti^{4+} for $Cu_{40}Ni_{60}$/C-T0, $Cu_{40}Ni_{60}$/C-TNS, and $Cu_{40}Ni_{60}$/C-TNSD. The Ti^{4+}:Ti^{3+} ratio for $Cu_{40}Ni_{60}$/C-TNSD indicates that about 50 % of the composite contains Ti^{3+} reduced species (see ca. 0.98:1 in Table 1). Compared to the catalysts prepared with TNS and T0 with a Ti^{4+}:Ti^{3+} ratio of 1.7:1 and 4.1:1 show a lower amount of Ti^{3+} species, i.e., 37% and 19%, respectively. It has been suggested that the excess electrons associated with each OV occupying Ti−3d orbitals can create Ti^{3+} sites [29]. Furthermore, the relative content of the reduced species and OVs in the O 1s region is higher for $Cu_{40}Ni_{60}$/C-TNSD than the other electrocatalysts. Therefore, it is fair to say that the C-TNSD has more OVs among the supports. No Ti 2p peak has been found for $Cu_{40}Ni_{60}$/C, as expected.

To this end, the XPS core O 1s spectra for the $Cu_{40}Ni_{60}$/C-TNSD, $Cu_{40}Ni_{60}$/C-TNS, $Cu_{40}Ni_{60}$/C-T0, and $Cu_{40}Ni_{60}$/C electrocatalysts are also presented in Fig. 3(d). The $Cu_{40}Ni_{60}$/C catalyst exhibited peaks at 530.3, 531.1, 532.0, and 533.0 eV assigned to the oxygen bonded to Ni and Cu metals (M − O), C−O, C]O compounds, and OVs, respectively [14,30]. Carbon does not contain oxygen atoms in its atomic structure; however, carbon vulcan can contain oxygen functional groups such as hydroxyl and carboxyl that could have

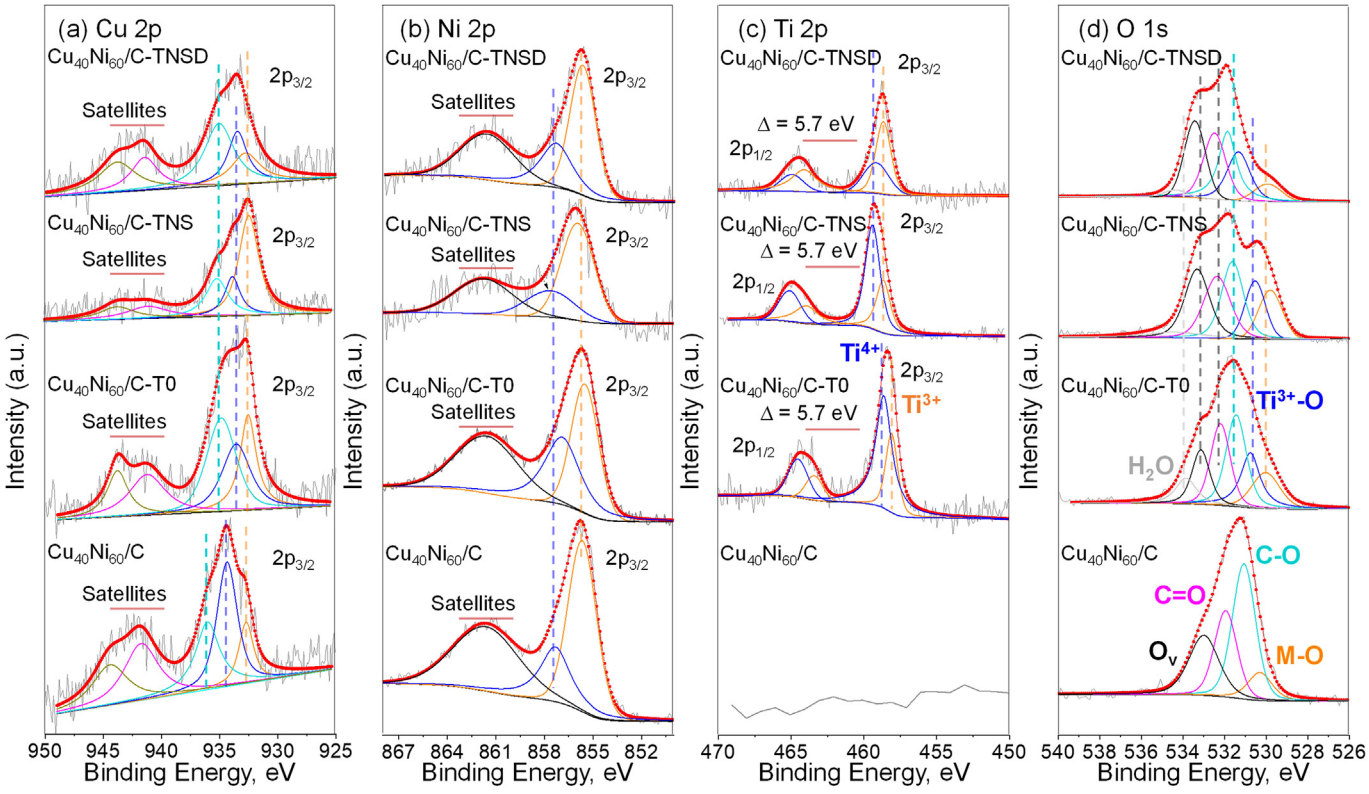

Fig. 3. XPS core spectra for the (a) Cu, (b) Ni, and (c) Ti 2p and (d) O 1s for $Cu_{40}Ni_{60}$/C, $Cu_{40}Ni_{60}$/C-T0, $Cu_{40}Ni_{60}$/C-TNS, and $Cu_{40}Ni_{60}$/C-TNSD.

Table 1
Specified contents of Ti^{3+} in the composites and the Ti^{4+}: Ti^{3+} ratio in the Ti 2p region.

Catalyst	Ti^{3+} (%) Ti 2p region	Ti^{4+}: Ti^{3+} Ti 2p region	Ti^{3+}+ Ov (%) O 1s region
$Cu_{40}Ni_{60}$/C-T0	19.7	4.1:1	31.5
$Cu_{40}Ni_{60}$/C-TNS	37.7	1.7:1	37.1
$Cu_{40}Ni_{60}$/C-TNSD	50.3	0.98:1	42.5

been reduced during the electrocatalyst support synthesis, creating Ov and other defects [31]. On the other hand, the samples containing TiO_2 showed peaks at about 530, 530.7, 531.4, 532.3, 533.3, and 534 eV that can be fitted with the oxygen bonded to Ti, Ni, and Cu metals (M − O), O—Ti^{3+} (following the Ti 2p results), C—O, C]O compounds, Ov, and adsorbed water, respectively [32].

In short, XRD, STEM, and XPS in Figs. 1, 2, and **3** reveal the presence of mixed oxides and hydroxides in CuNi. Although it is inconclusive, we should not disregard the presence of partially alloyed mixed co-catalyst phases (see STEM-EDX). Cu is encountered as Cu_2O and CuO, and Ni is present as an oxide. We should also not exclude that such species might hydroxylate after air exposure for XPS analysis. Furthermore, the presence of metal and metal oxide species has also been corroborated using cyclic voltammetry, as shown in Fig. S1. Overall, the structural and chemical characterization demonstrated the presence of Cu and Ni in the form of mixed species over C-TNS, C-TNSD, and C-T0.

3.3. Electrocatalytic characterization of C-TNS, C-TNSD, and C-T0

The electrocatalytic performance of the $Cu_{40}Ni_{60}$/C—TiO_2 is evaluated using cyclic voltammetry (CV) in the presence and absence of $NaNO_3$ in NaOH solution (Fig. 4). As seen in Fig. 4(a), the CV measurements show various redox peaks associated with Cu and Ni oxides for the various supports (e.g., C-TNS, C-TNSD, C-T0). Among the C—TiO_2, $Cu_{40}Ni_{60}$/C-TNS shows the lowest current toward Ni oxide within the potential window of 0.9—1.38 and 1.38—1.6 V vs. RHE and related to $Ni + 2OH^- \rightarrow Ni(OH)_2 + 2e^-$ and $Ni(OH)_2 + OH^- \rightarrow NiOOH + H_2O + e^-$, corresponding to redox peaks of oxidation and reduction, respectively [33]. For Cu/C (Fig. S1), a less pronounced peak within 0.82—0.88 V vs. RHE has been observed. Cu oxidized species can be associated with CuO and $Cu(OH)_2^-$. For other potentials, e.g., 0.52—0.59 V vs. RHE, the formation of Cu_2O is expected [34]. A detailed description is provided in the supporting **information section S1**. Overall, the proposed Cu and Ni metallic and oxidized species align with the species found with XRD, STEM-EDX, and XPS.

The electroreduction of NO_3^- performance of various CuNi electrocatalysts ratios are additionally evaluated using cyclic voltammetry in Fig. 4(b). In this case, $NaNO_3$ 0.1 M has been supplemented to the electrolyte to understand the electrochemical effect of NO_3^-. In the case of metals, particularly for CuNi electrocatalysts, the d-band center (ε_d) can be modulated for Ni 3d and N 2p orbitals. This modulation increases the energies of unoccupied anti-bonding N 2p states above the Fermi level [35]. The latest can lead to a favorable between the metallic surface and NOOH* intermediates, facilitating the selective formation of NH_3 by the reaction $NO_3^- + 6H_2O + 8e^- \rightarrow NH_3 + 9OH^-$. CuNi synergy makes the Cu 3d band move to a lower energy level, tuning the intermediates' energy adsorption [36].

3.4. NO_3-RR to NH_3

DEMS analyzes gaseous and volatile species [37] generated during the electrochemical NO_3^-RR [7]. The electrocatalytic activity of $Cu_{40}Ni_{60}$/C, $Cu_{40}Ni_{60}$/C-T0, $Cu_{40}Ni_{60}$/C-TNS, and $Cu_{40}Ni_{60}$/C-TNSD is shown in Fig. 5 (in blue). Measurements without $Cu_{40}Ni_{60}$ are also provided and colored in black. In Fig. 5, the faradaic current is recorded simultaneously with the ionic current (mass-signal) for (**a, g, m, s**) $m/z = 2$ assigned to H_2, (**b, h, n, t**) $m/z = 15$ for NO and NH_3, (**c, i, o, u**) $m/z = 17$ for NH_3, (**d, j, p, v**) $m/z = 30$ for NO, and (**e,k,q,w**) $m/z = 44$ for N_2O. N_2, NO_2, and NH_2OH mass signals have not been detected, although they have been observed in Pt or Pd electrocatalysts [6—8]. The corresponding faradaic current vs. potential profiles are shown in Fig. 5 (**f, l, r, x**).

Fig. 5 shows that the H_2 product has been observed for C and C—TiO_2supports(**a, g, m, s**). H_2 production is accompanied by a higher cell potential for C and C—TiO_2 in Fig. 5 (**f, l, r, x**). However, when $Cu_{40}Ni_{60}$ is loaded over C and C—TiO_2, a reduction in the cell potential is observed in Fig. 5 (**f, l, r, x**), accompanied by lower

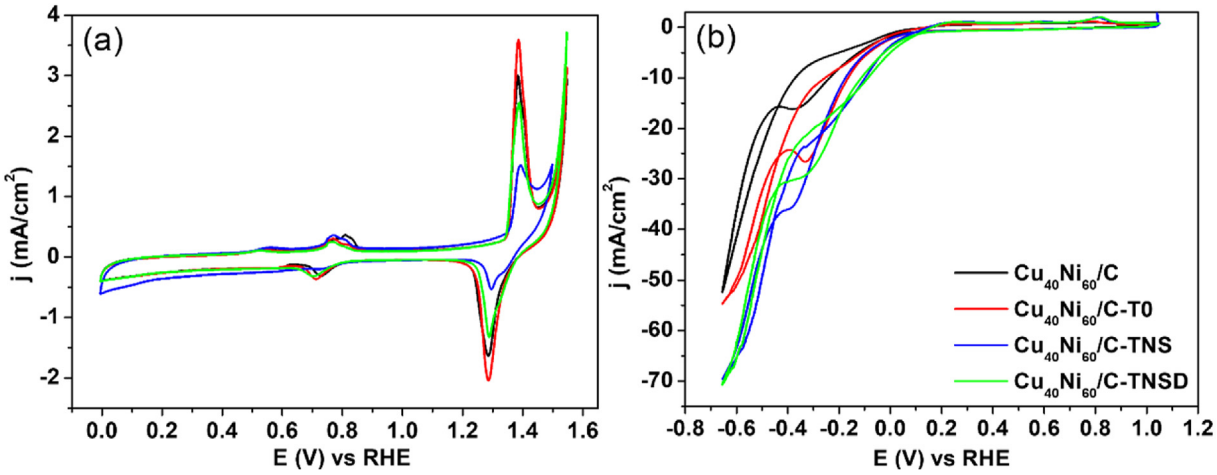

Fig. 4. (a) Current density-potential characteristics of $Cu_{40}Ni_{60}$/C and $Cu_{40}Ni_{60}$/C—TiO_2 in 1 M NaOH solution at a scan rate of 5 mV/s. (b) Current-potential characteristics of $Cu_{40}Ni_{60}$/C and $Cu_{40}Ni_{60}$/C—TiO_2 in 1 M NaOH and 0.1 M $NaNO_3$ at a scan rate of 20 mV/s.

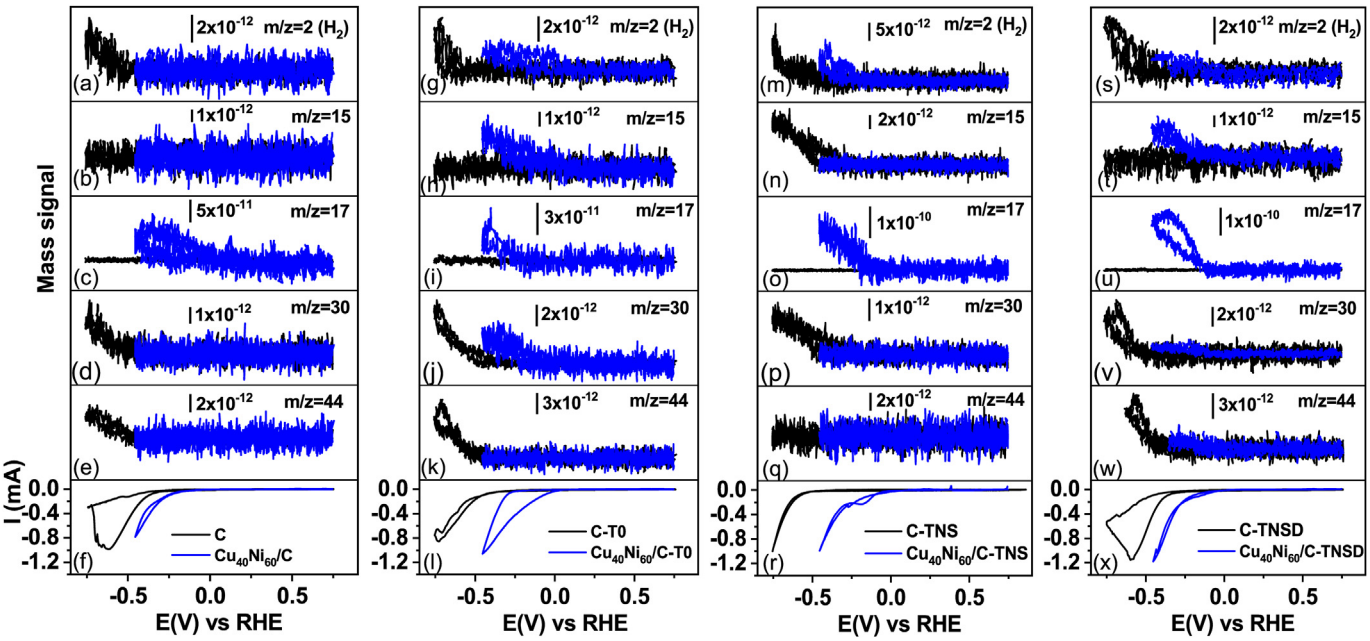

Fig. 5. Current-potential characteristics for (a, b, c, d, e, f) $Cu_{40}Ni_{60}$/C, (g, h, i, j, k, l) $Cu_{40}Ni_{60}$/C-T0, (m, n, o, p, q, r) $Cu_{40}Ni_{60}$/C-TNS, and (s, t, u, v, w, x) $Cu_{40}Ni_{60}$/C-TNSD 1 M NaOH with 0.1 M $NaNO_3$. Mass signal as a function of the applied potential (1 mV/s) for $m/z = 2$ (a, g, m, s), $m/z = 15$ (b, h, n, t), $m/z = 17$ (c, i, o, u), $m/z = 30$ (d, j, p, v) and $m/z = 44$ (e, k, q, w) are presented.

production of H_2 in Fig. 5 (**a, g, m, s**), indicating that $Cu_{40}Ni_{60}$ modifies the H^+ adsorption that leads to H_2 formation. In Fig. 5 (**b, h, n, t**) and (**c, i, o, u**), NH_3 has been found. However, owing to the overlap between NO and NH_3, $m/z = 15$ is not discussed. Hence, we analyze $m/z = 17$ to evaluate NH_3 production. In this case, $Cu_{40}Ni_{60}$/C-TNS and $Cu_{40}Ni_{60}$/C-TNSD have the highest NH_3 production among the electrocatalysts. It should be noted that C, C-T0, C-TNS, and C-TNSD did not produce NH_3. As for $Cu_{40}Ni_{60}$/C—Ti0 in Fig. 5 (d,j,p,v), additional ionic currents associated with NO ($m/z = 30$) have been observed at negative potentials with a further increase in NO content at higher negative potentials for C—TiO_2 supports only. Interestingly, no N_2O has been found in Fig. 5 (e,k,q,w) for $Cu_{40}Ni_{60}$/C, $Cu_{40}Ni_{60}$/C-T0, $Cu_{40}Ni_{60}$/C-TNS, and $Cu_{40}Ni_{60}$/C-TNSD. Among the supports, TNS did not show N_2O production, while a small amount of N_2O has been seen for C, C-T0, and C-TNSD. Small N_2O formation over TNSD can be related to the branching of oxygen atoms during NO_3-RR. Isotopic fractionation occurs at these branch points, leading to the preferential loss of O as water and the transfer of O to the subsequent NO_x products, which later form N_2O as a byproduct [38]. For comparison, a similar DEMS and electrochemical analysis to Fig. 5 is presented in Fig. S3 but in the absence of NO_3^-. The results reveal that H_2 is the most abundant product. Control experiments have been carried out using monometallic Cu and Ni catalysts in the presence of $NaNO_3$, as shown in Fig. S4. NH_3 is the main product of Cu, while Ni produces H_2. Variations in product selectivity can be related to a change in adsorption energies when contrasting CuNi with monometallic electrocatalysts, such as Cu, which favors NO_3-RR to NH_3, while Ni favors hydrogen evolution reaction (Fig. S4) [39]. Compared to Fig. S4, the CuNi synergy is evidenced by increased NH_3 production in Fig. 5.

The relative product selectivity for the various C and C—TiO_2 supports loaded with $Cu_{40}Ni_{60}$ presented in Fig. 6(a) and **6(b)** is estimated using the Faradaic and ionic current profile in Fig. S5. C, C-TNS, and C-TNSD support loaded with $Cu_{40}Ni_{60}$ reveal selectivity values higher than 95% for NH_3, while C-T0 remains below 90% selectivity values with a more considerable amount of H_2 and NO produced. For $Cu_{40}Ni_{60}$/C, $Cu_{40}Ni_{60}$/C-TNS, and $Cu_{40}Ni_{60}$/C-TNSD, NO, and N_2O product selectivity remain below 1%. Among them, $Cu_{40}Ni_{60}$/C-TNS has a significant H_2 production comparable to $Cu_{40}Ni_{60}$/C-T0. This is quite interesting as $Cu_{40}Ni_{60}$ and C-TNSD synergy aids in suppressing hydrogen. The effect can be indirectly assessed by looking at the NO_3-RR products in Fig. 6(a) and **(b)**. Product selectivity variations might indicate a reaction change due to the unique interactions between the bulk solution's ions and the defect-rich surface. This can be the case for uncoordinated defects in TiO_2 (see Table 1), such as OV, which improves the performance in electroreduction reactions [40] by suppressing parasitic reactions (e.g., HER) or enhancing selectivity through specific active sites. From the HER suppression effect in $Cu_{40}Ni_{60}$/C-TNSD, we can argue that defective TiO_2 contains low-coordinated Ti^{3+}, and thus, OVs can enhance electrical conductivity and promote electron transfer to maximize NH_3 production.

Another important point in Fig. 6(a) and **(b)** is the relatively high NH_3 selectivity of $Cu_{40}Ni_{60}$/C, $Cu_{40}Ni_{60}$/C-TNS, and $Cu_{40}Ni_{60}$/C-TNSD. In this case, the faradaic current demonstrated that $Cu_{40}Ni_{60}$/C-TNSD further increases NH_3 production (Fig. 6(c)), attributed to the synergistic effect between $Cu_{40}Ni_{60}$ and defect-rich support. Similar NH_3 production for $Cu_{40}Ni_{60}$/C-TNS is displayed. However, a plateau in the region from −0.2 to −0.3 mA has been found for $Cu_{40}Ni_{60}$/C-TNS, suggesting an electron transfer barrier over the electrocatalyst affecting electrochemical reaction (Fig. 6(d)), generating a large amount of byproducts like H_2 [41]. To this end, the electrocatalyst selectivity (Fig. 6(a)) is contrasted in Fig. S6. Cu demonstrates a higher selectivity toward NH_3 and Ni to H_2, as shown in Fig. S6(b). From our results, it is fair to say that $Cu_{40}Ni_{60}$/C-TNSD is a more suitable electrocatalyst due to a relatively large amount of NH_3 over time, as determined in Fig. 6(c) and chronoamperometry in Fig. S7.

Electrochemical surface area (ECSA) is measured (Fig. S8 and Fig. S9(a)) to generate insights into the catalyst active sites that lead to $Cu_{40}Ni_{60}$/C-TNSD having the highest Faradaic current. In Table 2, estimated ECSAs are shown. The ECSA values can be related to active sites that promote faradaic interactions over the electrocatalyst. The results demonstrated that $Cu_{40}Ni_{60}$/C-TNSD has the

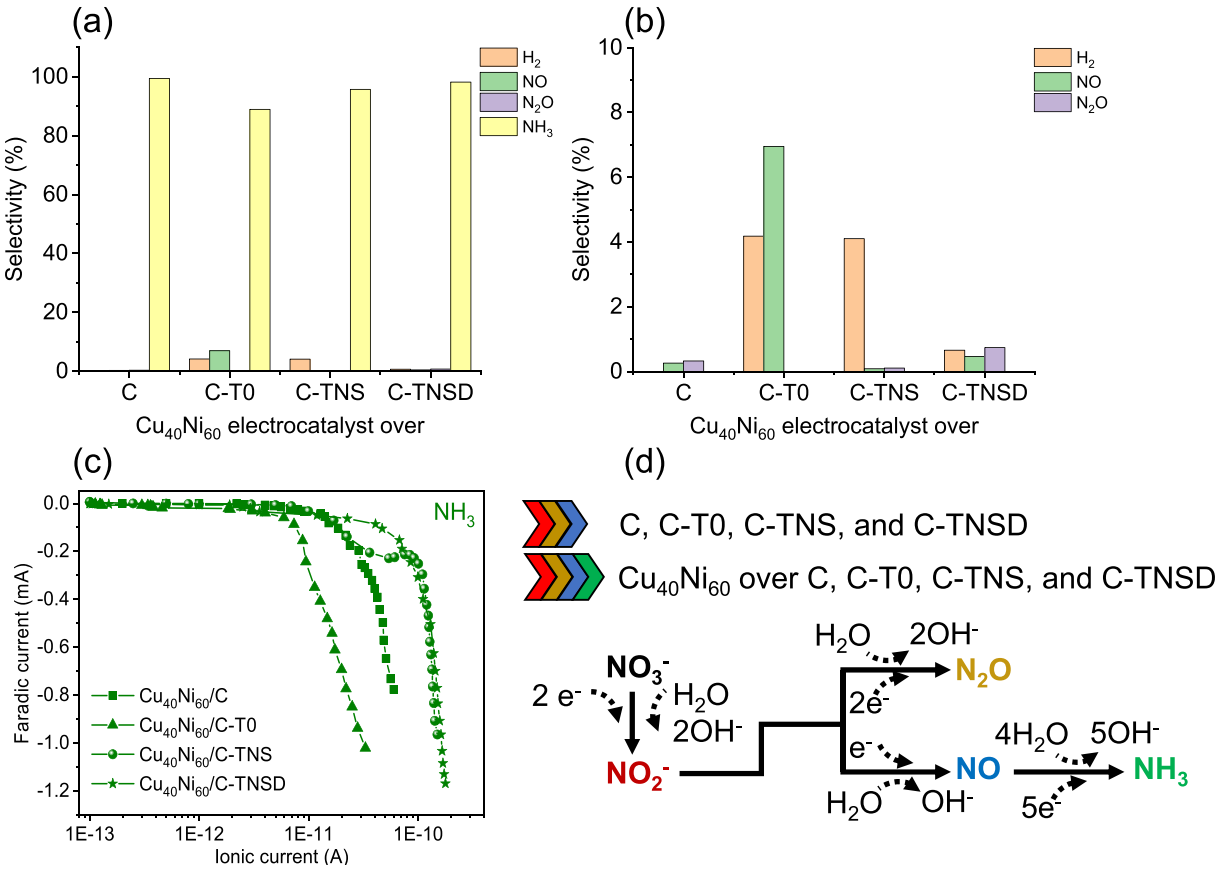

Fig. 6. (a)–(b) Relative selectivity estimated from DEMS Faradaic current vs. ionic current profiles of C–TiO_2 supports loaded with $Cu_{40}Ni_{60}$. Selectivity results have been estimated from Fig. S5. (c) Faradaic current vs. ionic current profiles from DEMS for the various supports loaded with $Cu_{40}Ni_{60}$. (d) Proposed chemical reaction pathway after sequential product evaluation.

Table 2
Electrochemical surface areas and capacitances for $Cu_{40}Ni_{60}$/C, $Cu_{40}Ni_{60}$/C-T0, $Cu_{40}Ni_{60}$/C-TNS, and $Cu_{40}Ni_{60}$/C-TNSD.

	$Cu_{40}Ni_{60}$/C	$Cu_{40}Ni_{60}$/C-T0	$Cu_{40}Ni_{60}$/C-TNS	$Cu_{40}Ni_{60}$/C-TNSD
ECSA ($cm^2/mg_{catalyst}$)	3.77	3.71	4.43	4.85
Capacitance (μF)	145.5	222.9	261.2	245.9

highest ECSA, while $Cu_{40}Ni_{60}$/C-TNS, $Cu_{40}Ni_{60}$/C-T0, and $Cu_{40}Ni_{60}$/C remain below 4.85 $cm^2/mg_{catalyst}$, indicating that the OVs induce anchoring sites for redox reactions [42].

The latest attributions are supported by estimating the electrochemical capacitance for the various C–TiO_2 electrocatalysts (Fig. S9(b) and Fig. S10). In this case, the highest capacitance has been found for $Cu_{40}Ni_{60}$/C-TNS, as shown in Table 2. $Cu_{40}Ni_{60}$/C-TNS value can be attributed to a significant affinity to adsorb H^+ species on the catalyst's surface (Fig. 6(b)). This behavior is related to the higher current magnitude in hydrogen adsorption observed in cyclic voltammograms in Fig. 4(a) and subsequent H_2 production in Fig. 5.

$Cu_{40}Ni_{60}$/C-TNSD showed the highest catalytic activity due to the improved charge transport due to uncoordinated sites, such as OVs, as shown with XPS in Fig. 3 and Table 1, which can additionally lead to an increase in ECSA (Table 2). The effect of C-TNSD is explored further by comparing the $Cu_{40}Ni_{60}$/C-TNSD and C-TNSD ECSA in Fig. S11, Fig. S12, and Table S1. $Cu_{40}Ni_{60}$/C-TNSD shows an ECSA of 4.85 $cm^2/mg_{catalyst}$, while C-TNSD ECSA is 4.22 $cm^2/mg_{catalyst}$. The results reveal that C-TNSD provides nearly 87% of the ECSA, while the remaining 13% is due to the presence of $Cu_{40}Ni_{60}$. Similar trends between supported and unsupported $Cu_{40}Ni_{60}$ metals have been found in Table S1. Our findings suggest that uncoordinated species in TiO_2, like Ti^{3+}, increase the ECSA. These sites can stimulate the OVs formation and be used as adsorption sites and as an effective charge transport medium influencing electronic behavior in $Cu_{40}Ni_{60}$/C-TNSD [40,43,44].

To this end, electrochemical impedance spectroscopy (EIS) is carried out to investigate the charge transport on the electrocatalyst surface and thus generate insights about $Cu_{40}Ni_{60}$ and C-TNSD synergy. EIS uses a small amplitude potential or current perturbation as a sinusoidal signal to excite the electrochemical system [45]. The corresponding Nyquist plots at NaOH solution without and with $NaNO_3$ are displayed in Fig. 7(a) and **7(b)**, respectively. The radius of the semicircle is related to the charge transfer resistance, and a smaller radius indicates a faster electron transfer at the interface [46]. As can be seen, it follows a quasi-semicircular behavior, indicating the presence of a capacitor-like behavior during charge transfer. The EIS results can be associated with an equivalent circuit representing the electrochemical electric elements. The resulting equivalent circuit often exhibits a frequency dispersion that simple elements cannot describe as resistances, capacitances, or inductances. This frequency dispersion is attributed to a distribution of the capacitances and can be

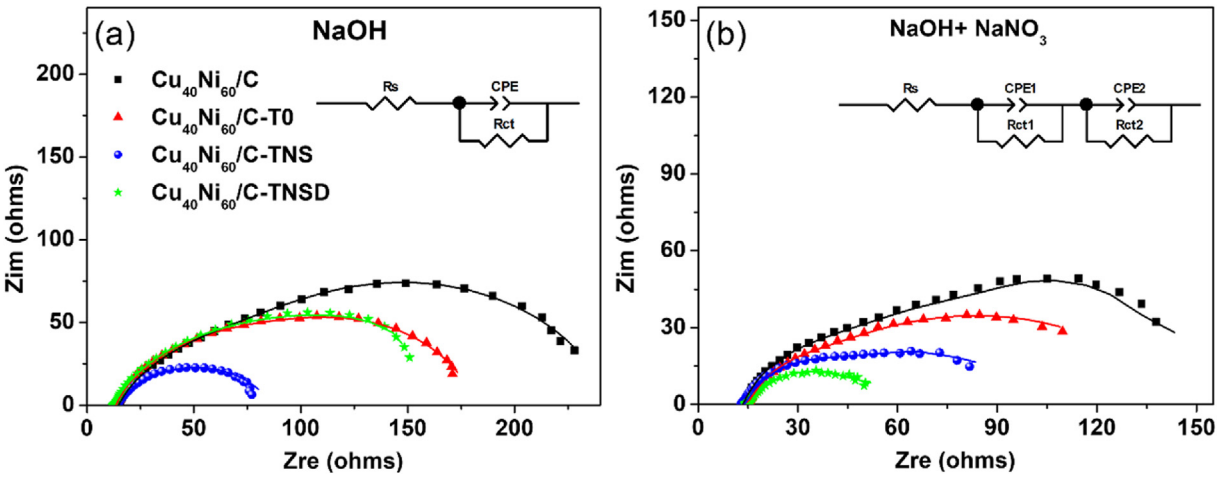

Fig. 7. Nyquist plots of CuNi/C–TiO_2 in (a) NaOH 1 M, and (b) NaOH 1 M and $NaNO_3$ 0.1 M.

Table 3
Electric parameters for $Cu_{40}Ni_{60}$/C, $Cu_{40}Ni_{60}$/C-TNS, and $Cu_{40}Ni_{60}$/C-TNSD.

NaOH Element	$Cu_{40}Ni_{60}$/C	$Cu_{40}Ni_{60}$/C-T0	$Cu_{40}Ni_{60}$/C-TNS	$Cu_{40}Ni_{60}$/C-TNSD
R_s	14.48	14.72	15.67	16.54
R_{ct}	123.70	98.91	69.46	114.01
CPE-T	0.001070	0.000715	0.001778	0.000878
CPE-P	0.76476	0.76876	0.72870	0.78660
$NaOH + NaNO_3$ Element	$Cu_{40}Ni_{60}$/C	$Cu_{40}Ni_{60}$/C-T0	$Cu_{40}Ni_{60}$/C-TNS	$Cu_{40}Ni_{60}$/C-TNSD
R_s	15.41	14.49	14.86	15.58
R_{ct1}	20.41	19.61	9.45	18.8
CPE1-T	0.000882	0.000988	0.005174	0.001415
CPE1-P	0.92092	0.90333	0.92269	0.88671
R_{ct2}	138.21	122.4	76.3	35.95
CPE2-T	0.00251	0.002789	0.004139	0.013382
CPE2-P	0.70188	0.64878	0.59789	0.46301

expressed in a constant-phase-element (CPE). CPE in an electrochemical system indicates a non-ideal capacitor [47]. In Fig. 7(a), the interaction with the catalyst implies the adsorption of H_2O molecules on the surface in the Volmer step given by equation (1) [48].

$$H_2O + e^- + M \rightleftharpoons MH_{ads} + OH^- \quad (1)$$

Where M is the metallic active site, hydrogen is subsequently formed with the available H_{ads}. Thus, the resistance of charge transfer (R_{ct}) that measures the efficiency of the charge transfer processes at an applied potential is in the following order for the various electrocatalysts: $R_{Cu40Ni60/C} > R_{Cu40Ni60/C\text{-}TNSD} > R_{Cu40Ni60/C\text{-}T0} > R_{Cu40Ni60/C\text{-}TNS}$ (Table 3). This can explain the HER promotion in $Cu_{40}Ni_{60}$/C-TNS (Fig. 6(b)). However, we should not exclude that such HER promotion is related to the C-TNS, known from XPS for its less defective character than TNSD (Fig. 3 and Table 1). With or without $Cu_{40}Ni_{60}$, TNS can increase the charge transport behavior, promoting H_2 [49]. In Fig. 7(b), NO_3^- is introduced and studied with EIS. In this case, adsorption/desorption processes are more efficient in the presence of defective electrocatalysts, giving a less limited charge transport. $Cu_{40}Ni_{60}$/C-TNSD exhibits a smaller semicircle than the other electrocatalysts. In this context, it could be seen that the EIS circuit equivalent shows two-time constants referring to a multi-step process simultaneously, where NO_3-RR and HER are involved. The multi-step process can involve the interaction of more intermediates converting NO_3^- to NO, N_2O, and NH_3 (Fig. 6). To this end, the trend of R_{ct1} values is $R_{Cu40Ni60/C} > R_{Cu40Ni60/C\text{-}T0} > R_{Cu40Ni60/C\text{-}TNSD} > R_{Cu40Ni60/C\text{-}TNS}$ and for R_{ct2}, the sequency is $R_{Cu40Ni60/C} > R_{Cu40Ni60/C\text{-}T0} > R_{Cu40Ni60/C\text{-}TNS} > R_{Cu40Ni60/C\text{-}TNSD}$. The results indicate that $Cu_{40}Ni_{60}$/C-TNSD has a higher affinity toward NO_3-RR, which predominates at low frequencies, as seen in the second time constant in Table 3. The latest results align with previous results, where uncoordinated species, like OVs, can be used as adsorption sites and as an effective charge transport medium influencing the electronic behavior of the $Cu_{40}Ni_{60}$/C-TNSD [40,43,44]. The results highlight the synergistic effect between $Cu_{40}Ni_{60}$ and C-TNSD, where $Cu_{40}Ni_{60}$ is aided by the support, which increases charge transport while suppressing HER.

4. Conclusions

CuNi electrocatalysts have been investigated to understand the synergistic effect between CuNi and the support during NO_3-RR in an alkaline medium. The catalysts prepared with the $Cu_{40}Ni_{60}$ wt% ratio modify the hydrogen adsorption while maintaining NO_3-RR selectivity to NH_3 uncompromised. $Cu_{40}Ni_{60}$ loaded on C-TNSD support increases charge transport while suppressing HER, which resulted in the most efficient electrocatalyst for NH_3 production. ECSA and capacitance values agree with the higher activity for $Cu_{40}Ni_{60}$/C-TNSD, demonstrating that uncoordinated defects, such as OVs, increase surface area. EIS indicates that the redox reaction

pathway is modified with NO_3^- favoring the increase of NH_3 productivity in $Cu_{40}Ni_{60}$/C-TNSD. The results align with DEMS, where $Cu_{40}Ni_{60}$/C-TNSD showed one of the highest selectivity, demonstrating the synergistic effect between an optimal CuNi ratio and defect-rich support. The results can incentivize the development of defect-rich electrocatalysts for NO_3-RR to NH_3.

CRediT authorship contribution statement

Eleazar Castañeda Morales: Data curation, Formal analysis, Investigation, Methodology, Validation, Visualization, Writing – original draft. **José Oziel Peralta Cruz:** Data curation, Formal analysis, Investigation, Methodology, Validation, Visualization. **Francisco Ruíz-Zepeda:** Formal analysis, Investigation, Methodology, Resources, Validation, Visualization. **Arturo Susarrey-Arce:** Resources, Supervision, Writing – original draft, Writing – review & editing. **Martha Leticia Hernández-Pichardo:** Project administration, Supervision, Writing – original draft, Writing – review & editing. **Arturo Manzo Robledo:** Project administration, Supervision, Writing – original draft, Writing – review & editing.

Declaration of competing interest

The authors declare that they have no known competing financial interests or personal relationships that could have appeared to influence the work reported in this paper.

Data availability

Data will be made available on request.

Acknowledgments

The authors acknowledge the Instituto Politécnico Nacional for the financial support received through projects SIP-20231007 and 20231003. The authors gratefully acknowledge the CNMN-IPN for the characterization of materials facilities. The authors, E. Castañeda Morales and J. O. Peralta Cruz acknowledge CONACYT-Mexico for a doctorate study fellowship.

Appendix B. Supplementary data

Supplementary data to this article can be found online at https://doi.org/10.1016/j.mtener.2024.101525.

References

[1] W. de Vries, Impacts of nitrogen emissions on ecosystems and human health: a mini review, Curr. Opin. Environ. Sci. Health 21 (2021) 100249, https://doi.org/10.1016/j.coesh.2021.100249.
[2] J.C. Ehlers, A.A. Feidenhans'l, K.T. Therkildsen, G.O. Larrazábal, Affordable green hydrogen from alkaline water electrolysis: key research needs from an industrial perspective, ACS Energy Lett. 8 (2023) 1502–1509, https://doi.org/10.1021/acsenergylett.2c02897.
[3] H. Xu, Y. Ma, J. Chen, W.X. Zhang, J. Yang, Electrocatalytic reduction of nitrate - a step towards a sustainable nitrogen cycle, Chem. Soc. Rev. 51 (2022) 2710–2758, https://doi.org/10.1039/d1cs00857a.
[4] H. Hirakawa, M. Hashimoto, Y. Shiraishi, T. Hirai, Selective nitrate-to-ammonia transformation on surface defects of titanium dioxide photocatalysts, ACS Catal. 7 (2017) 3713–3720, https://doi.org/10.1021/acscatal.7b00611.
[5] J. Lim, C.A. Fernández, S.W. Lee, M.C. Hatzell, Ammonia and nitric acid demands for fertilizer use in 2050, ACS Energy Lett. 6 (2021) 3676–3685, https://doi.org/10.1021/acsenergylett.1c01614.
[6] S. Vázquez-Bautista, E. Ramírez-Meneses, A. Manzo-Robledo, G. Zacahua-Tlacuatl, L. Lartundo-Rojas, J. Acosta-Jara, L.L. Pedraza-Segura, M. Luna-Trujillo, Electro-reduction of NOx-species in alkaline medium at modified carbon-supported palladium nanoparticles with variable concentration of C-sp2: an in-situ mass-spectrometry approach, Appl. Catal., B 320 (2023) 121984, https://doi.org/10.1016/j.apcatb.2022.121984.
[7] J. Soto-Hernández, C.R. Santiago-Ramirez, E. Ramirez-Meneses, M. Luna-Trujillo, J.A. Wang, L. Lartundo-Rojas, A. Manzo-Robledo, Electrochemical reduction of NOx species at the interface of nanostructured Pd and PdCu catalysts in alkaline conditions, Appl. Catal., B 259 (2019) 118048, https://doi.org/10.1016/j.apcatb.2019.118048.
[8] C.R. Santiago-Ramírez, J. Vera-Iturriaga, P. del Angel, A. Manzo-Robledo, M.L. Hernández-Pichardo, J. Soto-Hernández, DEMS and Raman study of the monatomic hydrogen adsorption during electro-reduction of NO3- and NO2- at Pt nanoparticles supported at W18O49-ZrO2-C nanocomposite, Appl. Catal., B 282 (2021) 119545, https://doi.org/10.1016/j.apcatb.2020.119545.
[9] O.Q. Carvalho, R. Marks, H.K.K. Nguyen, M.E. Vitale-Sullivan, S.C. Martinez, L. Árnadóttir, K.A. Stoerzinger, Role of electronic structure on nitrate reduction to ammonium: a periodic journey, J. Am. Chem. Soc. 144 (2022) 14809–14818, https://doi.org/10.1021/jacs.2c05673.
[10] L. Barrera, R. Silcox, K. Giammalvo, E. Brower, E. Isip, R. Bala Chandran, Combined effects of concentration, pH, and polycrystalline copper surfaces on electrocatalytic nitrate-to-ammonia activity and selectivity, ACS Catal. 13 (2023) 4178–4192, https://doi.org/10.1021/acscatal.2c05136.
[11] M.E. Chavez, M. Biset-Peiró, S. Murcia-López, J.R. Morante, Cu2O-Cu@Titanium surface with synergistic performance for nitrate-to-ammonia electrochemical reduction, ACS Sustain. Chem. Eng. 11 (2023) 3633–3643, https://doi.org/10.1021/acssuschemeng.2c05885.
[12] Y. Wang, W. Zhou, R. Jia, Y. Yu, B. Zhang, Unveiling the activity origin of a copper-based electrocatalyst for selective nitrate reduction to ammonia, Angew. Chem. Int. Ed. 59 (2020) 5350–5354, https://doi.org/10.1002/anie.201915992.
[13] A. Iarchuk, A. Dutta, P. Broekmann, Novel Ni foam catalysts for sustainable nitrate to ammonia electroreduction, J. Hazard Mater. 439 (2022) 129504, https://doi.org/10.1016/j.jhazmat.2022.129504.
[14] M.A. Rodriguez-Olguin, C. Flox, R. Ponce-Pérez, R. Lipin, F. Ruiz-Zepeda, J.P. Winczewski, T. Kallio, M. Vandichel, J. Guerrero-Sánchez, J.G.E. Gardeniers, N. Takeuchi, A. Susarrey-Arce, Chlorine in NiO promotes electroreduction of CO2 to formate, Appl. Mater. Today 28 (2022) 101528, https://doi.org/10.1016/j.apmt.2022.101528.
[15] L. Mattarozzi, S. Cattarin, N. Comisso, P. Guerriero, M. Musiani, L. Vázquez-Gómez, E. Verlato, Electrochemical reduction of nitrate and nitrite in alkaline media at CuNi alloy electrodes, Electrochim. Acta 89 (2013) 488–496, https://doi.org/10.1016/j.electacta.2012.11.074.
[16] L. Durivault, O. Brylev, D. Reyter, M. Sarrazin, D. Bélanger, L. Roué, Cu-Ni materials prepared by mechanical milling: their properties and electrocatalytic activity towards nitrate reduction in alkaline medium, J. Alloys Compd. 432 (2007) 323–332, https://doi.org/10.1016/j.jallcom.2006.06.023.
[17] Y. Wang, A. Xu, Z. Wang, L. Huang, J. Li, F. Li, J. Wicks, M. Luo, D.H. Nam, C.S. Tan, Y. Ding, J. Wu, Y. Lum, C.T. Dinh, D. Sinton, G. Zheng, E.H. Sargent, Enhanced nitrate-to-ammonia activity on copper-nickel alloys via tuning of intermediate adsorption, J. Am. Chem. Soc. 142 (2020) 5702–5708, https://doi.org/10.1021/jacs.9b13347.
[18] J. Zhao, L. Liu, Y. Yang, D. Liu, X. Peng, S. Liang, L. Jiang, Insights into electrocatalytic nitrate reduction to ammonia via Cu-based bimetallic catalysts, ACS Sustain. Chem. Eng. 11 (2023) 2468–2475, https://doi.org/10.1021/acssuschemeng.2c06498.
[19] Q. Zhang, Y. Li, M. Geng, J. Zhu, H. Sun, B. Jiang, Defect-engineered TiO2 nanotube cathode for nitrate reduction to ammonia and upcycling into (NH4)2SO4 in the paired electrolysis system, Appl. Catal., B 330 (2023) 122658, https://doi.org/10.1016/j.apcatb.2023.122658.
[20] T.S. Bui, E.C. Lovell, R. Daiyan, R. Amal, Defective metal oxides: lessons from CO2RR and applications in NOxRR, Adv. Mater. 35 (2023) 2205814, https://doi.org/10.1002/adma.202205814.
[21] Z. Wei, X. Niu, H. Yin, S. Yu, J. Li, Synergistic effect of oxygen defects and hetero-phase junctions of TiO2 for selective nitrate electroreduction to ammonia, Appl. Catal. Gen. 636 (2022) 118596, https://doi.org/10.1016/j.apcata.2022.118596.
[22] Z. Wang, S. Liu, X. Zhao, M. Wang, L. Zhang, T. Qian, J. Xiong, C. Yang, C. Yan, Interfacial defect engineering triggered by single atom doping for highly efficient electrocatalytic nitrate reduction to ammonia, ACS Mater. Lett. 5 (2023) 1018–1026, https://doi.org/10.1021/acsmaterialslett.3c00007.
[23] L. Liu, F. Gao, H. Zhao, Y. Li, Tailoring Cu valence and oxygen vacancy in Cu/TiO2 catalysts for enhanced CO2 photoreduction efficiency, Appl. Catal., B 134–135 (2013) 349–358, https://doi.org/10.1016/j.apcatb.2013.01.040.
[24] Q. Wu, L.D.L. Duchstein, G.L. Chiarello, J.M. Christensen, C.D. Damsgaard, C.F. Elkjær, J.B. Wagner, B. Temel, J.D. Grunwaldt, A.D. Jensen, In situ observation of Cu–Ni alloy nanoparticle formation by X-ray diffraction, X-ray absorption spectroscopy, and transmission electron microscopy: influence of Cu/Ni ratio, ChemCatChem 6 (2014) 301–310, https://doi.org/10.1002/CCTC.201300628.
[25] Y. Zhou, Z. Wang, Z. Pan, L. Liu, J. Xi, X. Luo, Y. Shen, Exceptional performance of hierarchical Ni–Fe (hydr)oxide@NiCu electrocatalysts for water splitting, Adv. Mater. 31 (2019) 1806769, https://doi.org/10.1002/adma.201806769.
[26] F.A. Akgul, G. Akgul, N. Yildirim, H.E. Unalan, R. Turan, Influence of thermal annealing on microstructural, morphological, optical properties and surface electronic structure of copper oxide thin films, Mater. Chem. Phys. 147 (2014) 987–995, https://doi.org/10.1016/j.matchemphys.2014.06.047.
[27] M. Grdeń, M. Alsabet, G. Jerkiewicz, Surface science and electrochemical analysis of nickel foams, ACS Appl. Mater. Interfaces 4 (2012) 3012–3021, https://doi.org/10.1021/am300380m.

[28] S. Wang, J. Cai, J. Mao, S. Li, J. Shen, S. Gao, J. Huang, X. Wang, I.P. Parkin, Y. Lai, Defective black Ti 3+ self-doped TiO 2 and reduced graphene oxide composite nanoparticles for boosting visible-light driven photocatalytic and photoelectrochemical activity, Appl. Surf. Sci. (2019) 467–468, https://doi.org/10.1016/j.apsusc.2018.10.138, 45–55.
[29] Z. Wei, X. Niu, H. Yin, S. Yu, J. Li, Synergistic effect of oxygen defects and hetero-phase junctions of TiO2 for selective nitrate electroreduction to ammonia, Appl. Catal. Gen. 636 (2022) 118596, https://doi.org/10.1016/j.apcata.2022.118596.
[30] M.P. Woods, E.J. Biddinger, P.H. Matter, B. Mirkelamoglu, U.S. Ozkan, Correlation between oxygen reduction reaction and oxidative dehydrogenation activities over nanostructured carbon catalysts, Catal. Lett. 136 (2010) 1–8, https://doi.org/10.1007/s10562-010-0304-5.
[31] C. Bittencourt, M. Hecq, A. Felten, J.J. Pireaux, J. Ghijsen, M.P. Felicissimo, P. Rudolf, W. Drube, X. Ke, G. Van Tendeloo, Platinum-carbon nanotube interaction, Chem. Phys. Lett. 462 (2008) 260–264, https://doi.org/10.1016/j.cplett.2008.07.082.
[32] R. Boppella, J.E. Lee, F.M. Mota, J.Y. Kim, Z. Feng, D.H. Kim, Composite hollow nanostructures composed of carbon-coated Ti3+ self-doped TiO2-reduced graphene oxide as an efficient electrocatalyst for oxygen reduction, J. Mater. Chem. A Mater. 5 (2017) 7072–7080, https://doi.org/10.1039/c7ta00583k.
[33] V.L. Oliveira, C. Morais, K. Servat, T.W. Napporn, P. Olivi, K.B. Kokoh, G. Tremiliosi-Filho, Kinetic investigations of glycerol oxidation reaction on Ni/C, Electrocatalysis 6 (2015) 447–454, https://doi.org/10.1007/s12678-015-0261-2.
[34] R. Bogdanowicz, J. Ryl, K. Darowicki, B.B. Kosmowski, Ellipsometric study of oxide formation on Cu electrode in 0.1 M NaOH, J. Solid State Electrochem. 13 (2009) 1639–1644, https://doi.org/10.1007/S10008-008-0650-Z/FIGURES/7.
[35] J. Cai, Y. Wei, A. Cao, J. Huang, Z. Jiang, S. Lu, S.Q. Zang, Electrocatalytic nitrate-to-ammonia conversion with ~100% Faradaic efficiency via single-atom alloying, Appl. Catal., B 316 (2022) 121683, https://doi.org/10.1016/j.apcatb.2022.121683.
[36] X. Lu, H. Song, J. Cai, S. Lu, Recent development of electrochemical nitrate reduction to ammonia: a mini review, Electrochem. Commun. 129 (2021) 107094, https://doi.org/10.1016/j.elecom.2021.107094.
[37] C.J. Bondue, M.T.M. Koper, A DEMS approach for the direct detection of CO formed during electrochemical CO2 reduction, J. Electroanal. Chem. 875 (2020) 113842, https://doi.org/10.1016/j.jelechem.2020.113842.
[38] K.L. Casciotti, J.K. Böhlke, M.R. McIlvin, S.J. Mroczkowski, J.E. Hannon, Oxygen isotopes in nitrite: analysis, calibration, and equilibration, Anal. Chem. 79 (2007) 2427–2436, https://doi.org/10.1021/ac061598h.
[39] K.K. Patra, P.A. Bharad, V. Jain, C.S. Gopinath, Direct solar-to-hydrogen generation by quasi-artificial leaf approach: possibly scalable and economical device, J. Mater. Chem. A Mater. 7 (2019) 3179–3189, https://doi.org/10.1039/C8TA11307F.
[40] Z. Wang, L. Wang, Role of oxygen vacancy in metal oxide based photoelectrochemical water splitting, EcoMat 3 (2021) e12075, https://doi.org/10.1002/eom2.12075.
[41] H. Wang, Y. Guo, C. Li, H. Yu, K. Deng, Z. Wang, X. Li, Y. Xu, L. Wang, Cu/CuOxIn-Plane heterostructured nanosheet arrays with rich oxygen vacancies enhance nitrate electroreduction to ammonia, ACS Appl. Mater. Interfaces 14 (2022) 34761–34769, https://doi.org/10.1021/acsami.2c08534.
[42] R. Jia, Y. Wang, C. Wang, Y. Ling, Y. Yu, B. Zhang, Boosting selective nitrate electroreduction to ammonium by constructing oxygen vacancies in TiO2, ACS Catal. 10 (2020) 3533–3540, https://doi.org/10.1021/acscatal.9b05260.
[43] S. Wendt, R. Schaub, J. Matthiesen, E.K. Vestergaard, E. Wahlström, M.D. Rasmussen, P. Thostrup, L.M. Molina, E. Lægsgaard, I. Stensgaard, B. Hammer, F. Besenbacher, Oxygen vacancies on TiO2(1 1 0) and their interaction with H2O and O2: a combined high-resolution STM and DFT study, Surf. Sci. 598 (2005) 226–245, https://doi.org/10.1016/j.susc.2005.08.041.
[44] W. Li, R. Liang, N.Y. Zhou, Z. Pan, Carbon black-doped anatase TiO2 nanorods for solar light-induced photocatalytic degradation of methylene blue, ACS Omega. 5 (2020) 10042–10051, https://doi.org/10.1021/acsomega.0c00504.
[45] S. Wang, J. Zhang, O. Gharbi, V. Vivier, M. Gao, M.E. Orazem, Electrochemical impedance spectroscopy, Nature. Reviews. Methods. Primers 1 (2021) 1–21, https://doi.org/10.1038/s43586-021-00039-w.
[46] H.S. Magar, R.Y.A. Hassan, A. Mulchandani, Electrochemical impedance spectroscopy (Eis): principles, construction, and biosensing applications, Sensors 21 (2021) 6578, https://doi.org/10.3390/s21196578.
[47] J.B. Jorcin, M.E. Orazem, N. Pébère, B. Tribollet, CPE analysis by local electrochemical impedance spectroscopy, in: Electrochim Acta, Pergamon, 2006, pp. 1473–1479, https://doi.org/10.1016/j.electacta.2005.02.128.
[48] K. Ojha, S. Saha, P. Dagar, A.K. Ganguli, Nanocatalysts for hydrogen evolution reactions, Phys. Chem. Chem. Phys. 20 (2018) 6777–6799, https://doi.org/10.1039/c7cp06316d.
[49] B. Hinnemann, P.G. Moses, J. Bonde, K.P. Jørgensen, J.H. Nielsen, S. Horch, I. Chorkendorff, J.K. Nørskov, Biomimetic hydrogen evolution: MoS2 nanoparticles as catalyst for hydrogen evolution, J. Am. Chem. Soc. 127 (2005) 5308–5309, https://doi.org/10.1021/ja0504690.